Applied Physics A (2020) 126:355
https://doi.org/10.1007/s00339-020-03504-7

Applied Physics A
Materials Science & Processing

S.I. : CURRENT STATE-OF-THE-ART IN LASER ABLATION

Effect of the spot size on ionization and degree of plasma shielding in plumes induced by irradiation of a copper target by multiple short laser pulses

Omid A. Ranjbar[1] · Zhibin Lin[2] · Alexey N. Volkov[1]

Received: 15 October 2019 / Accepted: 25 March 2020 / Published online: 21 April 2020

Abstract
The plasma plume expansion into argon background gas at atmospheric pressure induced by irradiation of a copper target with a burst of three short laser pulses at 266 nm wavelength is studied numerically for the laser spot diameters ranging from 20 µm to 500 µm. The computational model includes a thermal model of the irradiated target and a kinetic model of plume expansion. The kinetic model is implemented in the form of the direct simulation Monte Carlo method that is redesigned to account for ionization and absorption of laser radiation in the plume. The irradiation conditions are chosen to do not induce ionization and absorption during the first pulse in the burst independently of the laser spot size. During the second pulse, the ionization is initiated in the vicinity of the irradiated target behind the shock wave that is generated during that pulse and propagates through the vapor plume created by the preceding pulse. The simulations show that the degree of ionization and plasma shielding during the second and subsequent pulses strongly increases with increasing the laser spot size. It is explained by different rates of expansion between pulses in the plumes generated at various spot sizes. At a relatively small spot size, the rapid drop of density and temperature in the plume induced by the first pulse can preclude plasma ignition during the second and further pulses. These results suggest that the use of lasers with the spot sizes that are in the order of tens of micrometers can be favorable for mitigating the effect of plasma shielding in multi-pulse laser ablation when the plumes induced by individual laser pulses strongly interact with each other.

Keywords Laser ablation · Multi-pulse irradiation · Plume expansion · Laser spot size · Plasma shielding

1 Introduction

The formation of plasma in plumes induced by short-pulse laser radiation can strongly affect the effectiveness of laser processing of materials in such applications of laser ablation as drilling and patterning [1, 2], laser-induced breakdown spectroscopy [3, 4], pulsed laser deposition of functional thin films [5, 6], and laser shock peening [7]. In particular, the plasma plume can absorb a substantial part of laser energy. The absorption of laser radiation in the plume decreases the surface temperature and amount of ablated material, reducing the overall throughput and efficiency of laser processing of materials. This effect is commonly known as the plasma shielding or plasma screening effect [8, 9].

Current demands, e.g., of microelectronic industry, require fabrication of wafers or substrates with the size of individual surface features, e.g., the hole diameter or trench width, reduced to tens of micrometers. In laser processing, it can be achieved by reducing the laser spot size. Although it is generally accepted that the laser spot size can affect the expansion dynamics of plasma plumes, it appeares that the effect of the spot size on the degree of plasma shielding was not quantitatively analyzed. In experimental studies, it was shown that, with the variation of the spot size, the plume shape turns from a cylindrical-like to a spherical-like one [10, 11], and the degree of

✉ Alexey N. Volkov
avolkov1@ua.edu

Omid A. Ranjbar
oazadehranjbar@crimson.ua.edu

Zhibin Lin
linz@esi.com

[1] Department of Mechanical Engineering, University of Alabama, 7th Avenue, Tuscaloosa, AL 35487, USA

[2] MKS Instruments, Inc., 13900 NW Science Park Drive, Portland, OR 97229, USA

plasma shielding increases when the spot size decreases at constant pulse energy [11]. The case of constant peak fluence for spots of different sizes, however, was not considered. In multiple theoretical investigations of laser-induced plume expansion based on one-dimensional (1D) models, e.g., [12–15], the effects of the laser spot size could not be considered, since such models correspond to the case of infinitely large spot size. In numerical studies of two-dimensional (2D) plasma plume expansion, e.g., [16–20], the effects of variable spot size on the flow structure and plasma shielding effect were not systematically investigated.

The laser processing of metal targets is usually performed by multi-pulse irradiation with the pulse repetition rates varying from ~ 1 Hz to ~ 10 kHz. Higher repetition rates can be archived with the laser systems operating in the superpulse or double pulse mode, e.g., [21, 22], as well as in the burst mode, e.g., [23], when the laser pulses are grouped into trains or bursts with the intra-burst pulse repetition rate as high as ~ 100 MHz and much longer time delays between bursts. At high repetition rates, the plumes induced by individual pulses can interact with each other. The interaction between plumes can intensify plasma shielding, since the laser radiation from subsequent pulses propagates through plumes induced by preceding pulses. To the best of authors' knowledge, the interaction between plumes induced by multi-pulse irradiation is currently studied only based on 1D models, e.g., [24, 25], and the effect of the laser spot size on plasma shielding in the multi-pulse regime has not been discussed in previous theoretical and experimental works.

The goal of the present work is to study the degree of ionization and plasma shielding in plumes induced by multiple short laser pulses for the laser spot diameters varying from 20 μm to 500 μm under conditions when the plumes induced by individual pulses strongly interact with each other. To carry out such a study, we developed a computational kinetic model of laser-induced plasma plumes based on the direct simulation Monte Carlo (DSMC) method [26]. In our work, the DSMC method originally designed for simulations of neutral gas flows is modified in order to account for ionization and absorption processes. Our computational results indicate that the laser spot size is one of the key parameters that affect the degree of plasma shielding in multi-pulse laser ablation. In particular, we found that reducing the spot size can preclude the plasma ignition when the peak laser fluence and other irradiation parameters are fixed. The analysis of numerical results also suggests that the plasma ignition under conditions of multi-pulse irradiation can be controlled by changing the rate of overall plume expansion between pulses rather than heat accumulation in the irradiated target.

2 Computational model

The simulations are performed based on a hybrid computational model that includes a thermal model of the irradiated target, a kinetic model of flow in the plasma plume, as well as a model of laser radiation propagation and absorption inside the plume. The thermal model of the irradiated target is based on the 2D unsteady heat conduction equation that predicts the temperature field in the target and on its surface. The kinetic model of the two-component gas mixture flow is based on the Boltzmann kinetic equation [26–28]. It accounts for the effects of gas rarefaction and translational non-equilibrium in the plume flow and allows us to describe the structure of the Knudsen layer at the target surface subjected to strong evaporation and condensation. The kinetic model is implemented in the form of the DSMC method, when the gas flow is described by a large number of simulated particles that represent individual atoms or molecules in the real gas flow [26]. These particles participate in binary collisions, move between collisions, and interact with the interphase boundaries. The thermal model of the irradiated target and the kinetic model of the plume flow are coupled with each other through the boundary conditions that express the energy and mass balance at the irradiated surface. In particular, the local velocity of surface recession due to the net effect of evaporation and condensation is represented in the form $V_w = \left(\psi_e - \psi_c\right)/\rho$, where ρ is the target material density, ψ_e is the local mass flux density of atoms that evaporate from the surface, and ψ_c is the local mass density of atoms that condense at the surface. The evaporation flux density ψ_e is calculated based on the Hertz–Knudsen model of evaporation [28]. The condensation flux density ψ_c is calculated in the DSMC method by counting vapor atoms that return to the target surface from the plume. The interaction of the background gas atoms with the irradiated surface is described by the Maxwell model of diffuse scattering, e.g., [27]. The binary collisions between the vapor and background gas atoms are described by the variable hard sphere (VHS) molecular model. The simulations are performed with a computer code that was previously developed to study laser-induced plumes expanding from a plane target [29] and in cavities under conditions of spatial confinement [30, 31]. Further details on the thermal model and DSMC method, which are used in the present work, can be found in Ref. [31].

For simulations of plasma plume flows, we develop an extension of the classical DSMC method. This extension, which can be used in simulations based on both the equilibrium and non-equilibrium ionization models, is briefly discussed in Appendix 1. In the present work, however, the DSMC method is used together with the equilibrium ionization model, where the molar fractions of ions are calculated based on the Saha equations. The equilibrium ionization model is described in Appendix 2. The model of absorption of laser radiation by the plasma plume is based on Beer's law, where the linear absorption coefficient accounts for the effects of photoionization and inverse Bremsstrahlung (Appendix 2).

The simulations are performed for argon background gas and a bulk copper target irradiated by a pulsed laser at a wavelength of 266 nm. The laser beam is assumed to be normal to the irradiated surface. The axis of the laser beam is considered as the axis of symmetry for the target temperature field and flow in the plume. A single pulse of incident laser radiation has the smoothed flat-top temporal shape with the intensity in the spot center

$$I_{\mathrm{L}(p)}(t) = I_{\max}\begin{cases} \frac{1}{2}\left[1-\cos\left(\pi\frac{t}{\tau_{\mathrm{S}}}\right)\right], & 0 \le t < \tau_{\mathrm{S}}; \\ 1, & \tau_{\mathrm{S}} \le t \le \tau_{\mathrm{L}}-\tau_{\mathrm{S}}; \\ \frac{1}{2}\left[1+\cos\left(\pi\frac{t+\tau_{\mathrm{S}}-\tau_{\mathrm{L}}}{\tau_{\mathrm{S}}}\right)\right], & \tau_{\mathrm{L}}-\tau_{\mathrm{S}} < t \le \tau_{\mathrm{L}}; \\ 0, & t \le 0 \text{ or } t \ge \tau_{\mathrm{L}}, \end{cases} \tag{1}$$

where t is the time, τ_{L} is the pulse duration, τ_{S} is the smoothing time, $I_{\max} = F_{\mathrm{L}}/\left(\tau_{\mathrm{L}}-\tau_{\mathrm{S}}\right)$ is the maximum laser intensity at the spot center, and F_{L} is the peak laser fluence. The transversal mode of the laser beam is assumed to be Gaussian, and the distribution of laser intensity across the laser spot is given by the equation

$$I_{\mathrm{L}(p)}(r,t) = I_{\mathrm{L}(p)}(t)\exp\left(-\frac{r^2}{2\sigma_r^2}\right), \tag{2}$$

where r is the radial coordinate counted from the spot center, $\sigma_r = D_{\mathrm{L}}/\left(2\sqrt{2\log 2}\right)$, D_{L} is the laser spot diameter (FWHM), and the total pulse energy is equal to $E_{\mathrm{L}} = 2\pi\sigma_r^2 F_{\mathrm{L}}$. For a group or "burst" consisting of N_{L} individual pulses with the peak-to-peak separation τ_{pp}, the laser intensity is defined as

$$I_{\mathrm{L}}(r,t) = \sum_{m=1}^{N_{\mathrm{L}}} I_{\mathrm{L}(p)}\left(r, t-(m-1)\tau_{\mathrm{pp}}\right). \tag{3}$$

The thermal and optical properties of the irradiated material, as well as parameters of the VHS molecular model for copper vapor and argon, are identical to those that are used in Ref. [31]. The additional parameters of the ionization and radiation absorption models are given in Appendix 2.

3 Results and discussion

To reveal the effects of the laser spot size on the characteristics of laser-induced plasma plumes, we perform a series of simulations with the fixed laser pulse duration $\tau_{\mathrm{L}} = 30$ ns (smoothing time $\tau_{\mathrm{S}} = 3$ ns), pulse peak-to-peak separation $\tau_{\mathrm{pp}} = 60$ ns, peak fluence at the spot center $F_{\mathrm{L}} = 12.35$ J cm^{-2}, and variable laser spot diameter D_{L}. These irradiation conditions are chosen to ensure strong interaction between plumes produced by individual pulses and to avoid ionization in the plume during the first pulse in the burst. The simulations are performed at a background gas pressure of 1 bar and initial temperature of the target and the background gas equal to 300 K for $D_{\mathrm{L}} = 20$ μm ($E_{\mathrm{L}} = 0.056$ mJ), $D_{\mathrm{L}} = 150$ μm ($E_{\mathrm{L}} = 3.15$ mJ), and $D_{\mathrm{L}} = 500$ μm ($E_{\mathrm{L}} = 35$ mJ). The simulations under such conditions allow us to investigate how the interaction between plumes affects the ionization and plasma shielding effects during the second and subsequent pulses at various laser spot sizes. It is worth noting that the problem considered in the present work is different from the problems considered experimentally in Refs. [10, 11], where the effect of the laser spot size was investigated under conditions of constant pulse energy, so that decreasing spot size results in larger laser energy density and stronger ionization in the plume.

Under conditions of fixed peak fluence, the surface temperature and amount of the evaporated material at the spot center during the first pulse only marginally depend on D_{L}, but the overall rate of plume expansion and plume characteristics are strongly affected by the spot size. Figure 1 shows the distributions of the plume number density along the axis of flow symmetry obtained in a case of neutral plume flows induced by single laser pulses at $D_{\mathrm{L}} = 20$ μm, $D_{\mathrm{L}} = 150$ μm, and $D_{\mathrm{L}} = 500$ μm. In these simulations, the effects of ionization and laser radiation absorption are not accounted for. The black curves in Fig. 1 are calculated in a 1D simulation of plume expansion and correspond to the limiting case when $D_{\mathrm{L}} \to \infty$. These curves are obtained based on a 1D model previously developed and used in Ref. [25]. By a time of 30 ns (Fig. 1a), when the pulse ends, the distributions of number density obtained for relatively large spot diameters of 150 μm and 500 μm practically coincide with the distribution obtained in the 1D simulation. For these spot sizes, the distributions of plume temperature and macroscopic velocity also agree well with the corresponding distributions found in the 1D simulation. At the same time, the number density distribution obtained for $D_{\mathrm{L}} = 20$ μm strongly deviates from the

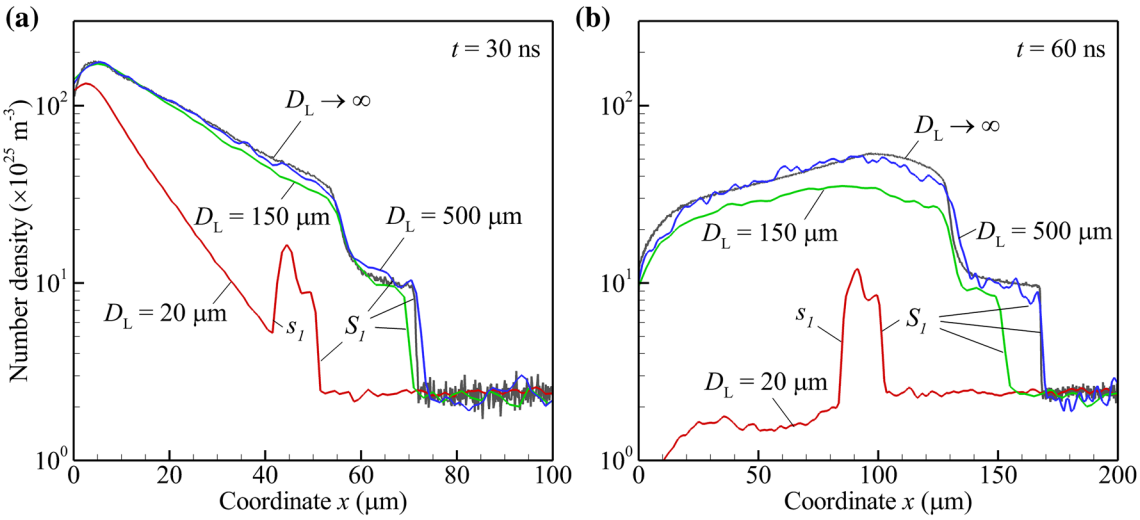

Fig. 1 Distributions of mixture number density at the axis of symmetry obtained at a time of 30 ns (**a**) and 60 ns (**b**) in simulations of a neutral plume expansion induced by a single laser pulse for the laser spot diameter $D_L = 20$ μm (red curves), $D_L = 150$ μm (green curves), and $D_L = 500$ μm (blue curves). The black curves are obtained based on a 1D model [25] and correspond to the case when $D_L \to \infty$. All simulations are performed with the same peak fluence at the spot center $F_L = 12.35$ Jcm^{-2}. S_1 and s_1 mark the primary and secondary shock waves (color figure online)

distribution established in the 1D simulation. Although all considered cases are characterized by practically the same plume density at the irradiated surface, the density in the plume obtained at $D_L = 20$ μm drops much faster with increasing distance from the surface than in cases of larger D_L. At $D_L = 20$ μm, the primary shock wave S_1 that propagates ahead of the plume in the background gas also moves slower and has a much smaller intensity. At a given time, the overall disagreement between 1D and 2D simulations decreases with increasing spot size. For instance, by a time of 60 ns (Fig. 1b), the position of the shock wave S_1 at $D_L = 150$ μm is already substantially different from the position of the shock wave obtained in the 1D simulation, while the shock waves obtained at $D_L = 500$ μm and in the 1D simulation still have the same position and intensity. With further increase in time, the distributions of plume parameters along the axis of symmetry in a case of $D_L = 500$ μm also begin to deviate from the corresponding distributions predicted by the 1D model.

For any finite spot size, with increasing time, the average density and temperature in the plume drop faster than it is predicted by the 1D model. It can be explained by a gradual change in the shape of the plume. Once the plume is formed, the "vertical" plume size x_M in the direction normal to the irradiated surface (x_M is some nominal coordinate of the mixing layer, where the vapor mixes with background gas, at the axis of symmetry) is much smaller than the characteristic radius of the plume in the lateral direction r_M. The latter has an order of $D_L/2$. Under such conditions, flow around the axis of symmetry is close to 1D flow, the primary shock wave has small curvature at the axis of symmetry, and the average density in the plume along the axis of symmetry drops with time as $1/x_M$. During further expansion, the vertical size of the plume increases faster than its lateral size, so eventually the vertical and lateral sizes become close to each other, $x_M \sim r_M$, while the primary shock wave and the mixing layer attain a characteristic quasi-hemispherical shape with much larger curvature at the axis of symmetry. The flow in the plume along the axis of symmetry is then affected by the curvature of the shock wave, the volume of the plume increases proportionally to x_M^2, and the average vapor density drops as $1/x_M^2$. Thus, the gradual deviation of the plume flow along the axis of symmetry from corresponding 1D flow can be described as a transition from a plane-like expansion when $x_M \ll r_M \sim D_L$ to a spherical-like expansion when $x_M \gtrsim r_M$. This transition occurs for any finite spot size, so that the distributions of plume parameters along the axis of symmetry in 2D flows can be approximated by the 1D model only during some limited initial time t_{1D}. This time increases with increasing laser spot diameter, but t_{1D} remains quite short even for relatively large D_L. For instance, if one assumes that the deviation between 2D and 1D simulations occurs when the positions of the primary shock waves differ from each other in 10%, then, under conditions considered in Fig. 1, $t_{1D} = 14$ ns at $D_L = 20$ μm, $t_{1D} = 64$ ns at $D_L = 150$ μm, and $t_{1D} = 206$ ns at $D_L = 500$ μm. The simulations, thus, show that t_{1D} varies roughly proportionally to D_L.

At $t \gg t_{1D}$, the average plume density and temperature, as well as the plume density and temperature in the vicinity of the irradiated surface, become substantially smaller than

the corresponding values predicted by 1D simulations. It can affect the plasma ignition threshold, which depends on the maximum temperature and density in the plume. As a result, the degree of plasma shielding, which can be measured by the fraction of laser energy absorbed by the plume, depends on the laser spot size. Under conditions of multi-pulse irradiation, when the plumes induced by individual pulses interact with each other, the effect of the laser spot size on the degree of plasma shielding can be even stronger than in the case of single-pulse irradiation. This preliminary reasoning agrees with the results of simulations performed for plasma plumes induced by multi-pulse laser radiation.

In Figs. 2 and 3, the temperature and total pressure fields (the total pressure is the sum of ion/atom and electron pressures) obtained in simulations of plasma plumes induced by a 3-pulse burst for various D_L are shown for a time of 90 ns and 150 ns, respectively. These time instants correspond to the ends of the second and third pulses in the burst. In the figures, S_n indicates the primary shock wave induced by n-th pulse ($n = 1, 2, 3$). The primary shock wave S_1 travels through the background gas, while other primary shocks initially propagate through the vapor plumes induced by preceding pulses. The plume of ablated material is bounded by the mixing layer, where the copper vapor partially diffuses through the background gas. In Figs. 2 and 3, the mixing layer is marked by letter "M" and shown by two black curves corresponding to its nominal boundaries, where the vapor molar fraction is equal to 99% and 1%.

In 1D simulations of neutral plumes induced by multi-pulse laser radiation [25] and plasma plumes induced by double pulses [24], it was shown that, under conditions of sufficiently large background gas pressure, the primary shock waves induced by subsequent pulses move faster than the shock waves induced by preceding pulses, so eventually these multiple shock waves merge. The larger velocity of subsequent shocks is primarily explained by the fact that these shock waves propagate through the high-temperature gas created by preceding pulses where the sound speed is

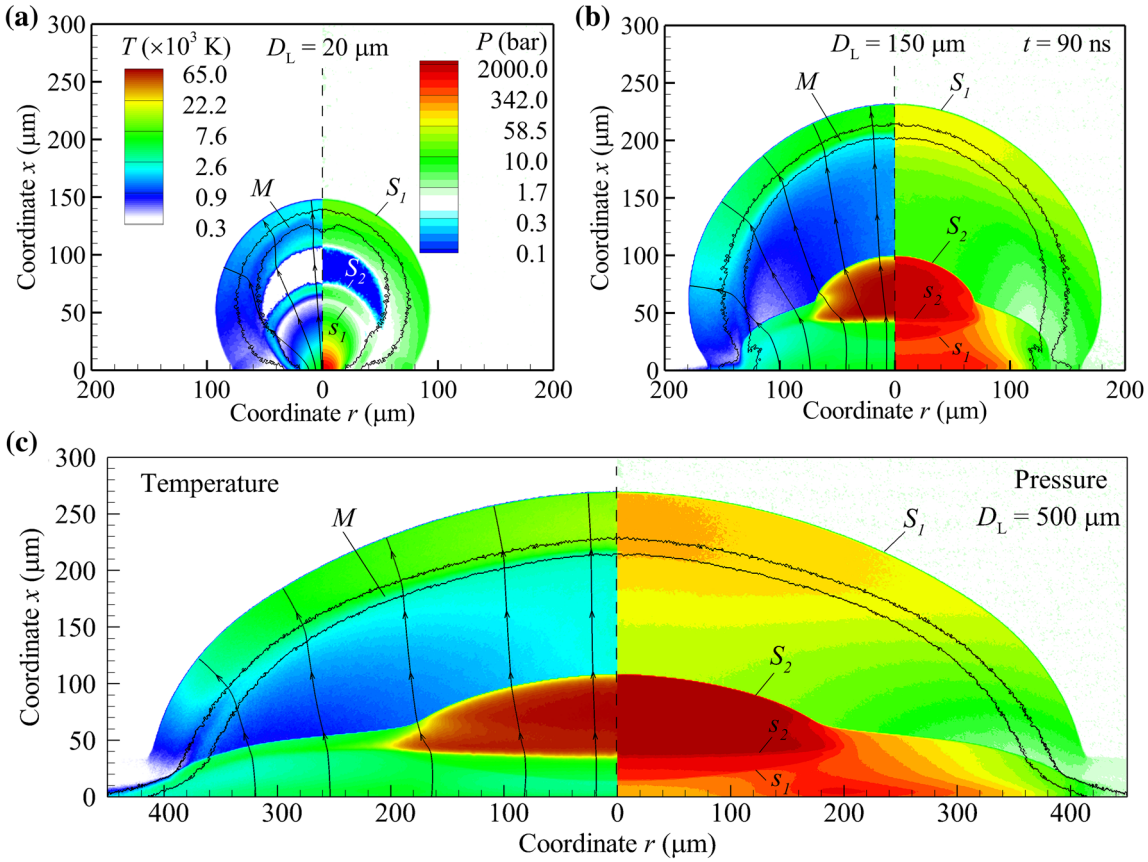

Fig. 2 Temperature (fields to the left from the axis of symmetry) and total pressure (fields to the right from the axis of symmetry) in the plasma plumes at a time of 90 ns induced by a 3-pulse burst and obtained for the laser spot diameter $D_L = 20$ μm (**a**), $D_L = 150$ μm (**b**), and $D_L = 500$ μm (**c**). S_n and s_n mark the primary and secondary shock waves induced by n-th pulse and M marks the mixing layer. The mixing layer is shown by two black curves. Between these curves the molar fraction of vapor varies from 99% to 1%. In the temperature fields, the streamlines of the mixture velocity field are shown by black curves with arrows. White in the color tables corresponds to the initial background gas temperature (300 K) and pressure (1 bar). The time $t = 90$ ns corresponds to the end of the second pulse in the burst

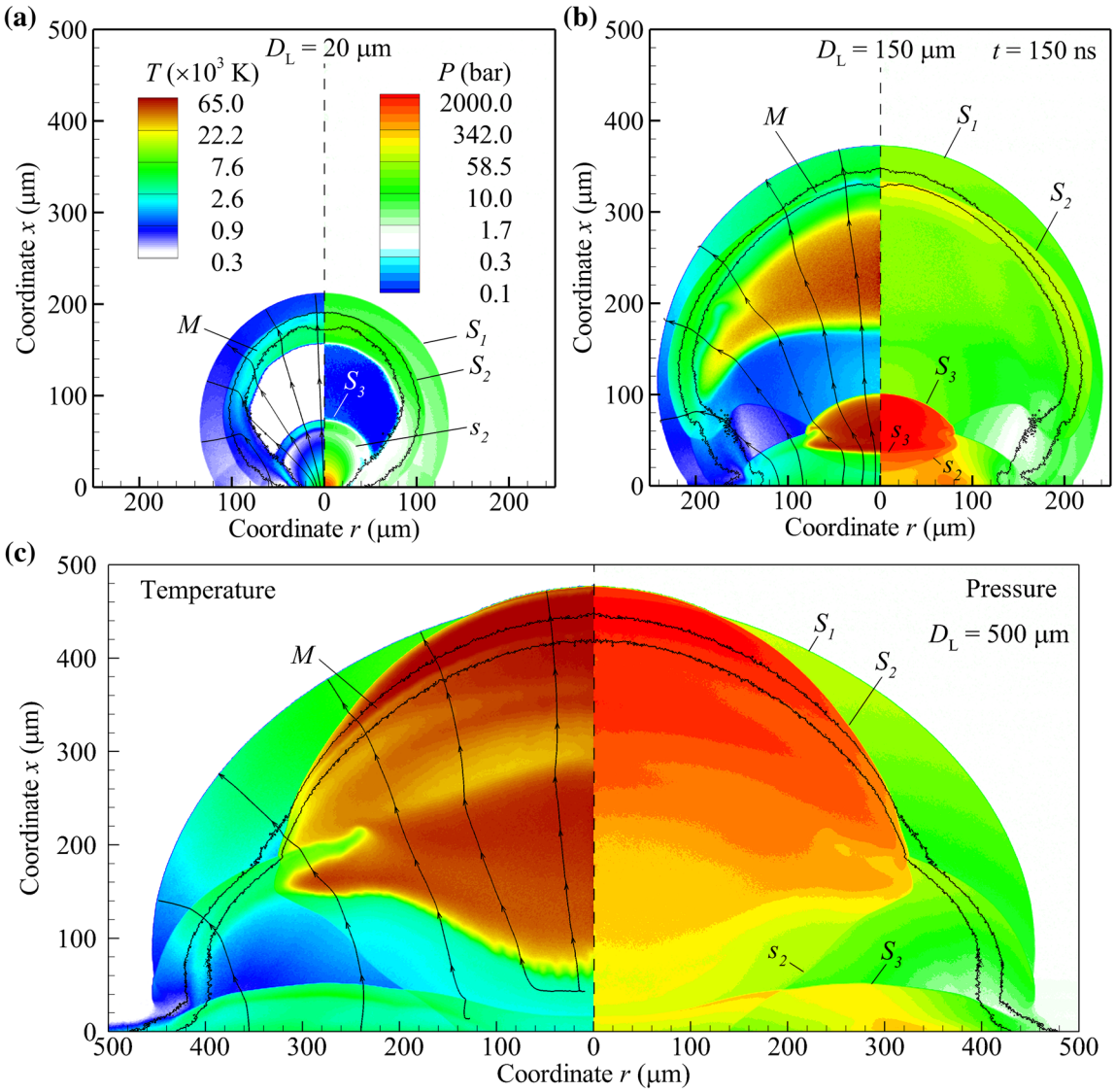

Fig. 3 Temperature (fields to the left from the axis of symmetry) and total pressure (fields to the right from the axis of symmetry) in the plasma plumes at a time of 150 ns induced by a 3-pulse burst and obtained for the laser spot diameter D_L = 20 μm (**a**), D_L = 150 μm (**b**), and D_L = 500 μm (**c**). S_n and s_n mark the primary and secondary shock waves induced by n-th pulse and M marks the mixing layer. The time t = 150 ns corresponds to the end of the third pulse in the burst. Further details are given in the caption of Fig. 2

higher [25] and by larger pressure ratio on the subsequent shocks [24]. Based on results shown in Figs. 2 and 3, one can conclude that a similar process of merging the primary shock waves is also observed in 2D simulations. In the practically neutral plume obtained at D_L = 20 μm (Figs. 2a and 3a), the second shock wave S_2 propagates through the relatively hot vapor created by the first pulse and gradually approaches S_1. The arrival of the third pulse results in repeating the process: The new shock wave S_3 moves with even higher velocity and finally merges with S_1 and S_2. The difference between the maximum plume temperature in two consecutive pulses tends to increase with increasing pulse number. For plasma plumes obtained at D_L = 150 μm (Figs. 2b and 3b) and 500 μm (Figs. 2c and 3c), the velocities of subsequent shock waves can be further increased compared to velocities of preceding shock waves due to absorption of laser radiation in the plumes. For instance, in the case of D_L = 500 μm, the velocity of shock S_2 with respect to shock S_1 increases as a result of absorption of laser radiation in the plasma region formed behind S_2. The release of the absorbed energy behind S_2 strongly increases the local plume temperature and pressure. It leads, in turn, to increasing the intensity and velocity of S_2.

The fast expansion of the ablation products, which is accompanied by the drop of pressure, also results in the formation of the secondary shock waves that propagate, in

the frame of reference moving with the local gas velocity, toward the target [24, 32]. In Fig. 1, this secondary shock wave s_1 is seen only in the distributions obtained for $D_L = 20$ μm. In Figs. 2 and 3, the secondary shock produced by n-th pulse is marked with s_n. These secondary shock waves are located close to the boundaries of the plasma regions, which face the irradiated target (Fig. 4). The interaction between multiple primary and secondary shock waves induced by multi-pulse irradiation results in a complicated flow structure in the plumes.

The irradiation conditions considered in this work correspond to a small degree of ionization and plasma shielding during the first pulse independently of D_L, so that the laser intensity incident to the surface during the first pulse is only marginally different from the incoming laser intensity. The conditions in the plume during the second pulse are more favorable for the onset of ionization. The degree of ionization in the plumes can be estimated from Fig. 4, where the number density fields of electrons and heavy particles are shown for a time of 150 ns, and Fig. 5, where the distributions of the electron number density along the axis of symmetry obtained for $D_L = 150$ μm and $D_L = 500$ μm are compared with each other. As one can see, at $D_L = 20$ μm, the plume practically consists of neutral atoms, while

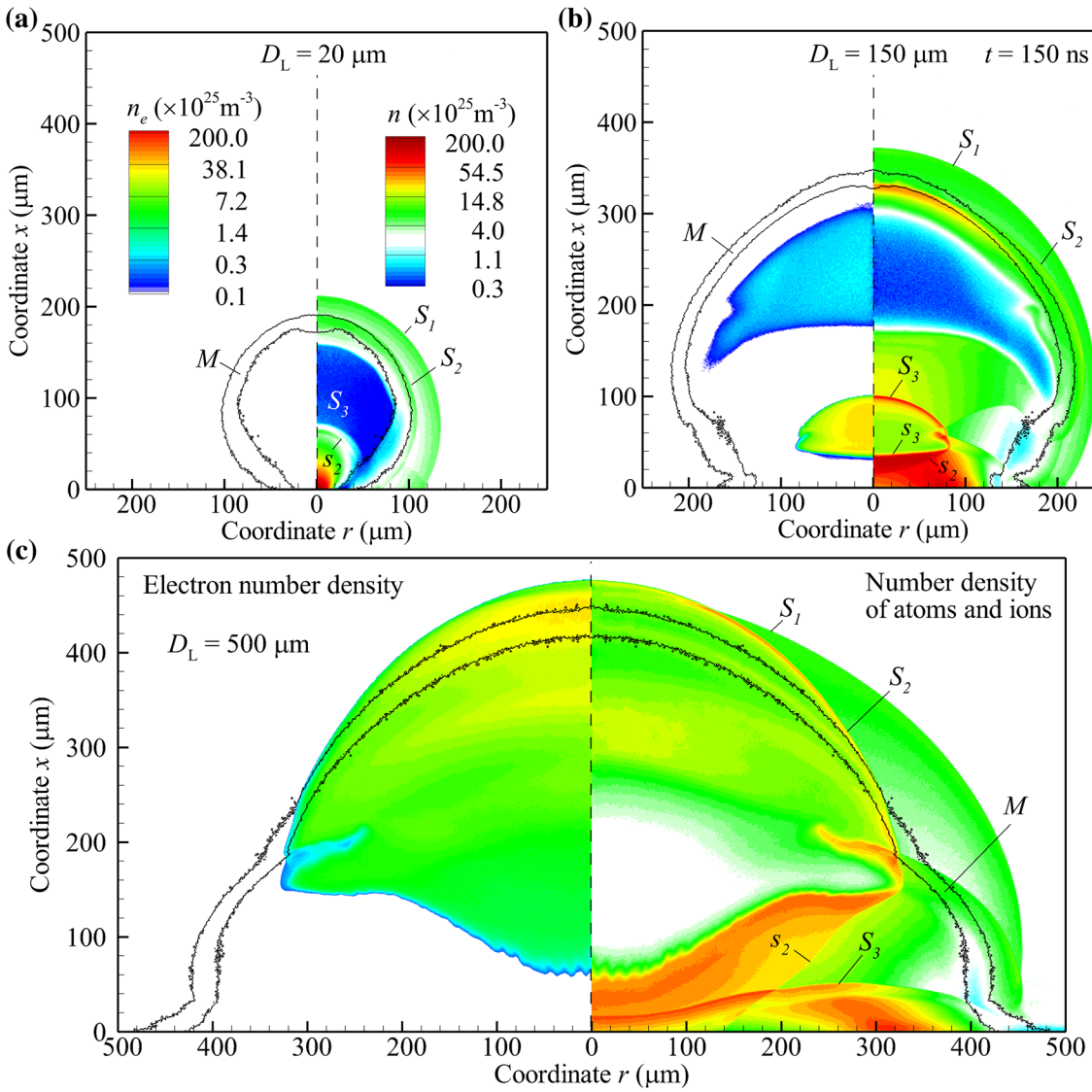

Fig. 4 Number densities of electrons (fields to the left from the axis of symmetry) and heavy particles (fields to the right from the axis of symmetry) in plasma plumes at a time of 150 ns induced by a 3-pulse burst and obtained for the laser spot diameter $D_L = 20$ μm (**a**), $D_L = 150$ μm (**b**), and $D_L = 500$ μm (**c**). S_n and s_n mark the primary and secondary shock waves induced by n-th pulse and M marks the mixing layer. Further details are given in the caption of Fig. 2

a substantial ionization develops in the plumes obtained at $D_L = 150$ µm and 500 µm. The difference between the target surface temperatures at the beginning of the second pulse obtained for various spot sizes is small and cannot explain the strongly different degrees of ionization in the corresponding plumes. For instance, the surface temperature at the spot center at the beginning of the second pulse is equal to 3050 K at $D_L = 20$ µm, 3200 K at $D_L = 150$ µm, and 3300 K at $D_L = 500$ µm at $t = 60$ ns.

In the case of the smallest spot size considered ($D_L = 20$ µm, Fig. 2a), by the time of the beginning of the second pulse, the primary shock wave S_1 attains a quasi-hemispherical shape. On the contrary, the size of the plume flow in the direction normal to the surface in the case of the largest sport size ($D_L = 500$ µm, Fig. 2c) for the same t is still smaller than the corresponding laser spot radius. In this case, the curvature of the primary shock wave is much smaller and, accordingly, much higher temperatures and densities are retained near the surface by the time of arrival of the second pulse compared to the case of the smallest spot.

For relatively large spot diameters, the plume density behind the second shock S_2 becomes sufficiently high to induce photoionization. For small spot diameters, on the contrary, the second shock wave cannot raise the density in the plume behind the shock front to levels supporting the onset of ionization. For instance, at $t = 65$ ns, the number density in the plume induced by the first pulse behind the second primary shock wave is equal to 0.6×10^{25} m^{-3} at $D_L = 20$ µm, 12×10^{25} m^{-3} at $D_L = 150$ µm, and 17×10^{25} m^{-3} K at $D_L = 500$ µm. The energy absorbed by the plume due to photoionization results in a further increase in the temperature behind S_2 and induces further ionization in this region of the plume. The formation of plasma with a relatively high density of electrons right behind the shock wave S_2 at $t = 75$ ns can be seen in Fig. 5a. The high-pressure and high-temperature plasma "bubble" behind S_2 expands in the directions both to and from the irradiated surface (Fig. 2b and c). The strong absorption of laser radiation by plasma and corresponding raise in the plasma pressure induce the secondary shock waves s_n that propagate toward the irradiates surface. These secondary shocks are much stronger than the secondary shocks in the neutral gas flows, e.g., shown in Fig. 2a for $D_L = 20$ µm. The secondary shock waves that appear as a result of absorption of laser radiation in the plume, e.g., shock wave s_2 in Fig. 3c, can fall on the target surface, while we did not observe interaction of weak secondary waves with the surface of the irradiated target in neutral plumes under the same irradiation conditions. The plasma bubble provides the major contribution to overall plasma shielding during the second pulse, when 28% and 51% of the incoming laser energy at the axis of symmetry is absorbed by the plasma plume at $D_L = 150$ µm and $D_L = 500$ µm, correspondingly (Fig. 6). The lateral size of the plasma bubble is about the laser spot radius, so that the strong plasma shielding inside the plasma region results in the formation of the local minimum of laser energy at the spot center (Fig. 7).

Thus, under considered conditions, the process of plasma ignition in the plume during the second pulse, which occurs near the surface and behind the shock wave generated by that pulse, is only marginally affected by changes in the thermal state of the target between the first and second pulses, but it is dominated by the conditions in the plume created by the first pulse near the target surface at the time when the second pulse arrives. These conditions, in turn, depend on the rate of overall plume expansion between pulses. It predetermines the strong effect of the spot size on the plasma formation and the overall plasma shielding effect.

At $D_L = 20$ µm, an additional increase of the surface temperature at the beginning of the third pulse up to 3600 K due to the thermal accumulation effect does not overcome the strong drop of the vapor density and temperature in the plume between the second and third pulses. In this case, the simulations predict only a marginal degree of plasma shielding during the whole 3-pulse burst (Fig. 6). The flow fields shown in Figs. 2a, 3a, and 4a, thus, correspond to the neutral gas flow.

By the end of the second pulse ($t = 90$ ns), the size of the plasma region and the electron number density distributions at the axis of symmetry obtained at $D_L = 150$ µm and $D_L = 500$ µm are only slightly different. The further simulations in these two cases continued until the arrival of the third pulse reveal, however, two different scenarios.

At $D_L = 150$ µm, the plasma region expands relatively fast. It induces a strong drop in the temperature, as well as in the number densities of heavy particles and electrons. In particular, the electron number density decreases in about an order of magnitude (Fig. 5c). This low-density plasma cannot strongly absorb the laser energy from the third pulse. The corresponding region of low-density plasma is shown in shades of blue in Fig. 4b. The major fraction of laser energy is absorbed in a new plasma region P_3, which appears near the irradiated surface behind the shock wave S_3 (Fig. 5d and e). The number density in this plasma plume and its thickness in the direction normal to the irradiated surface are larger than those for the plasma plume P_2 that is formed during the second pulse, so that the amount of laser density absorbed in the vicinity of the axis of symmetry during the third pulse increases up to 52% (Fig. 6).

At $D_L = 500$ µm, the density and temperature in the plasma plume P_2 remain sufficiently high by the time when the third pulse arrives. The major fraction of the incoming laser energy from the third pulse is absorbed in this plume, so that only 6% of laser energy reaches the surface at the

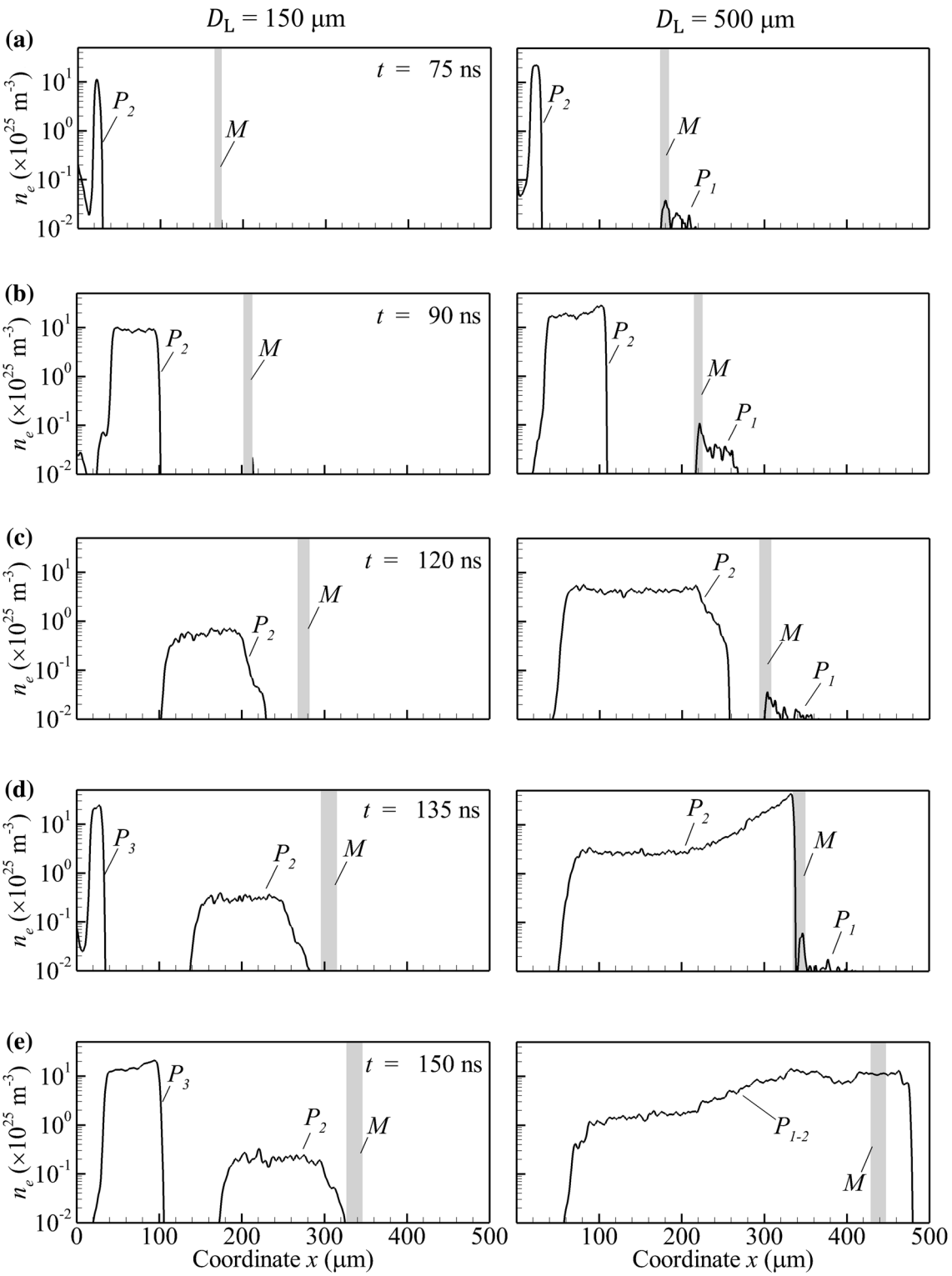

Fig. 5 Distributions of the electron number density along the axis of symmetry at a time of 75 ns (**a**), 90 ns (**b**), 120 ns (**c**), 135 ns (**d**), and 150 ns (**e**) induced by a 3-pulse burst and obtained for the laser spot diameter D_L = 150 μm (left column) and D_L = 500 μm (right column). The gray bars with letters "*M*" indicate the positions of the mixing layer where the molar fraction of copper vapor varies from 99% to 1%. P_n marks the plasma region that is initially formed during *n*-th pulse

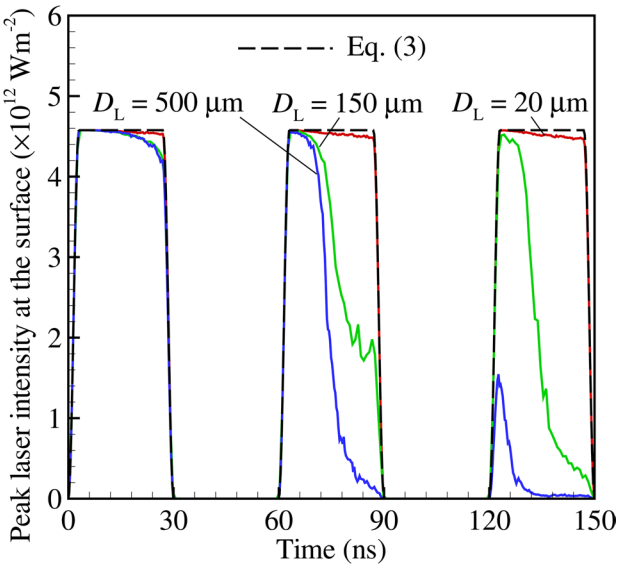

Fig. 6 Peak laser intensity incident to the irradiated surface versus time obtained in simulations with a 3-pulse burst at the laser spot diameter $D_L = 20$ μm (red solid curve), $D_L = 150$ μm (green solid curve), and $D_L = 500$ μm (blue solid curve). The black dashed curve corresponds to the incoming laser intensity $I_L(0, t)$ given by Eq. (3) (color figure online)

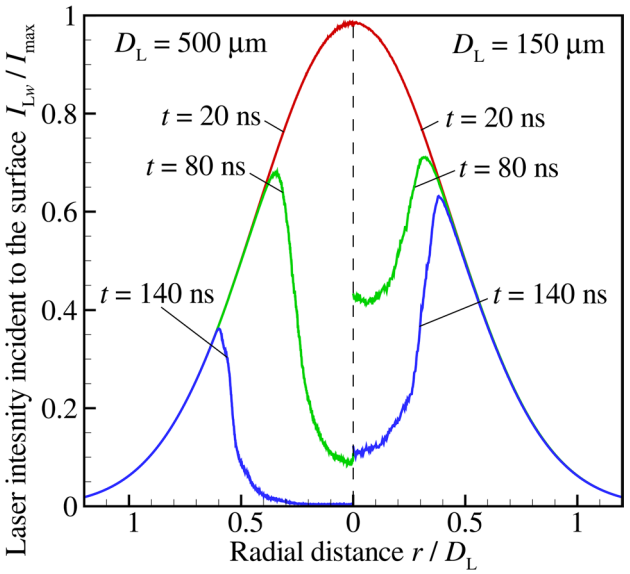

Fig. 7 Distributions of laser intensity incident to the irradiated target $I_{Lw} = I(0, r, t)$ along the target surface obtained in simulations for $D_L = 150$ μm (distributions to the right from the axis of symmetry at $r = 0$) and $D_L = 500$ μm (distributions to the left from the axis of symmetry) at a time $t = 20$ ns (red curves), 80 ns (green curves), and 140 ns (blue curves) (color figure online)

beam axis (Fig. 6). This energy is not enough to induce intensive evaporation at the center of the beam, and the additional plasma region does not appear. For instance, by the end of the third pulse, the target surface temperature at the spot center raises in this case only up to 5300 K compared to 9400 K at $D_L = 150$ μm. The large pressure inside the plume P_2 results in its rapid expansion and in increasing the plume thickness (Fig. 5d). It also increases the intensity and velocity of the shock wave S_2. When this shock wave moves through the mixing layer between the vapor and background gas, the temperature and density behind the shock wave appear to be sufficiently high to induce ionization of the background gas. By the end of the third pulse, the shock waves S_1 and S_2 already merge at the axis of symmetry and the plasma domain extends through argon up to the merged shock (Figs. 4c and 5e). The shock wave S_3 in this case is relatively weak and has an S-type shape, since the most intensive evaporation occurs at the edge of the plasma cloud cross section, $r/D_L \sim 0.5$, where the intensity of laser radiation incident to the surface is maximum (Fig. 7).

4 Conclusions

The 2D numerical simulations of plasma plumes induced by irradiation of a copper target by a burst of three short laser pulses are performed under conditions, when the first pulse does not induce ionization and radiation absorption in the plume, so that the plasma formation and absorption of laser radiation during subsequent pulses are determined by the rate of plume expansion between pulses and interaction between plumes produced by individual pulses. Then the initial ionization occurs in the plume close to the irradiated surface behind the shock wave that propagates through the plume created by a preceding laser pulse and the degree of plasma shielding strongly depends on the laser spot size. In a case of relatively small spot sizes, the ionization and absorption of incident laser radiation may not occur during the second and subsequent pulses as well, since the plume between pulses expands quasi-spherically, and the density and temperature in the plume drop fast. With increasing laser spot diameter, the plume expansion process in the vicinity of the axis of symmetry demonstrates a gradual transition from a quasi-spherical expansion to a planar one between pulses. The latter is characterized by a much slower drop in density and temperature. In this case, the shock wave generated by the second pulse can create temperature and density behind the shock front, which are sufficiently high to induce intensive ionization and absorption of laser radiation. As a result, in our simulations, during the second pulse, the amount of laser energy absorbed in the vicinity of the laser beam axis increases from 0.9% for 20 μm laser spot diameter to 28% for 150 μm spot diameter, and to 51% for 500 μm spot diameter.

Once the plasma region appears, the absorption of laser radiation from the subsequent pulses also strongly depends on the laser spot size, which affects the rate of plasma decay during the expansion of the plume between pulses. The rate

of plasma decay observed in our simulations can be dependent on the peculiarities of the current computational model that assumes equilibrium degrees of ionization and, therefore, may somewhat overestimate the rate of plasma decay between pulses. The general computational framework for simulations of laser-induced plasma plumes developed in the present paper based on the DSMC method, however, is compatible with both the equilibrium and non-equilibrium ionization models. In our future work, we plan to investigate the non-equilibrium ionization effects on the interaction between plasma plumes induced by multi-pulse laser radiation.

Acknowledgements This work is supported by the MKS Instruments, Inc. and NSF (Award CMMI-1554589). The computational support is provided by the Alabama Supercomputer Center.

Appendix 1. Direct simulation Monte Carlo method for plasma plume flows

The extension of the DSMC method for simulations of laser-induced plasma plume flows is developed to capture the most important effects of ionization and radiation absorption on the energy budget. The approach developed for simulations of plasma flows is based on the assumption of locally neutral plasma, which allows one to do not consider the electrons as simulated particles. Instead, one can assume that electrons move together with their parent ions and are characterized only by the electron temperature T_e. Moreover, in our approach, we use a method of "lumped" particles, when a single simulated particle in the DSMC method represents neutral atoms and ions of the same species with various charges z ($z = 0, \ldots, Z_{max}$, where eZ_{max} is the maximum ion charge considered in simulations, e is the charge of an electron). This is the extension of the approach adopted in the classical DSMC method, where every simulated particle represents W identical particles in the real gas flow (W is referred to as the statistical weight; usually $W \gg 1$). Then, in plasma flows, one can assume that a single simulated particle i of species s_i ($s_i = 1$ for vapor and $s_i = 2$ for the background gas) simultaneously represents WX_i^z ions with charges z, where X_i^z is the molar fraction of corresponding ions ($z = 0, \ldots, Z_{max}$; $\sum_z X_i^z = 1$). Thus, the current state of any simulated particle is defined by its translational velocity $\mathbf{v}_i$, molar fractions of ions X_i^z, and temperature of electrons $T_{e,i}$ associated with this particle. In the course of a simulation, values of X_i^z and $T_{e,i}$ are updated due to ionization and recombination process, as well as radiation absorption. This approach can be straightforwardly implemented in virtually any DSMC code.

In order to implement collisions between heavy particles, as well as ionization and absorption processes, the computational domain is divided into a mesh of cells. If a cell of volume V contains N simulated particles, then the number density n^z of ions with charge z, number density of electrons n_e, macroscopic velocity $\mathbf{u}$, electron energy density E_e, thermal energy density of heavy particles E_a, and total thermal energy density E, which includes the energy of ionization, in this cell can be calculated as follows

$$n^z = \frac{W}{V}\sum_{i=1}^{N} X_i^z, \tag{4a}$$

$$n_e = \frac{W}{V}\sum_{i=1}^{N}\sum_{z=1}^{Z_{max}} zX_i^z, \tag{4b}$$

$$\mathbf{u} = \sum_{i=1}^{N} m_i\mathbf{v}_i \Big/ \sum_{i=1}^{N} m_i, \tag{4c}$$

$$E_e = \frac{W}{V}\sum_{i=1}^{N}\sum_{z=1}^{Z_{max}} \frac{3}{2} zX_i^z k_B T_{e,i}, \tag{4d}$$

$$E_a = \frac{W}{V}\sum_{i=1}^{N} \frac{m_i\left(\mathbf{v}_i - \mathbf{u}\right)^2}{2}, \tag{4e}$$

$$E = E_a + E_e + \frac{W}{V}\sum_{i=1}^{N}\sum_{z=1}^{Z_{max}} X_i^z \sum_{m=1}^{z} \mathrm{IP}_{s_i}^m, \tag{4f}$$

where m_i is the mass particle i, IP_s^z is the z-th ionization energy of species s, and k_B is the Boltzmann constant. Each time step of the computational algorithm includes four major sub-steps: (1) Motion of particles, which leads to the redistribution of particles between cells, (2) binary collisions between heavy particles in cells, (3) absorption of laser radiation in cells, (4) ionization and recombination of particles in cells.

During the motion step, we account for the effect of electron pressure that is important in laser-induced plasma plumes. This effect is usually taken into account in hydrodynamic models of plasma plume expansion, e.g., [12–15]. For this purpose, we calculate the averaged electron temperature $T_e = E_e/\left((3/2)n_e k_B\right)$ and pressure $p_e = n_e k_B T_e$ in each cells and then determine numerically the gradient of the electron pressure ∇p_e. The equation of motion for every simulated particle in the form

$$m_i \frac{\mathrm{d}\mathbf{v}_i}{\mathrm{d}t} = -\frac{1}{n_a}\nabla p_e, \tag{5}$$

where $n_a = WN/V$ is the total number density of heavy particles, is solved numerically with the second-order Runge–Kutta method. Binary collision between heavy

particles is implemented based on the approach used in simulations of neutral gas flows [26].

The developed computational framework for simulations of plasma flows based on the modified DSMC method can be used for simulations of non-equilibrium plasma flows, where the local degrees of ionization are determined by the kinetic rates of ionization and recombination, e.g., [12], and the election temperature differs from the temperature of heavy particles $T_a = E_a/\left((3/2)n_a k_B\right)$. In the present paper, however, the developed approach is used assuming the equilibrium degrees of ionization predicted by the Saha equations and $T_a = T_e$.

The propagation of laser radiation through the plasma plume is described by Beer's law in the form $dI/dx = \alpha I$, where $I = I(x, r, t)$ is the intensity of laser radiation in a point with coordinates (x, r) at time t (x is the coordinate counted along the laser beam from the irradiated surface and r is the radial coordinate counted from the laser beam axis along the target surface), and α is the plasma linear absorption coefficient. In the present work, the absorption coefficient is calculated in each cell of the computational mesh based on the model presented in Appendix 2. The equation of radiation transfer is solved with the initial condition $I(x, r, t) \to I_L(r, t)$ at $x \to \infty$. The amount of energy, which is absorbed in a unit volume of a cell during a time step of duration Δt, is then equal to $\Delta E = \Delta t \alpha I$. This quantity is used to update thermal velocities of heavy particles in the cell according to the equation

$$\mathbf{v}_i^* = \mathbf{u} + \left(\mathbf{v}_i - \mathbf{u}\right)\sqrt{\frac{E_a + \Delta E}{E_a}}, \tag{6}$$

so that the total thermal energy density and temperature of heavy particles in the cell calculated based on the updated velocities $\mathbf{v}_i^*$ are equal to $E^* = E + \Delta E$ and $T^* = E^*/\left((3/2)n_a k_B\right)$.

The value of E^* and number densities of each species n_s are then used to find the updated fractions of ions $X_{(s)}^{z**}$ and temperature T^{**} in the cell based on the solution of the Saha equations coupled with the equations that express the energy balance, local neutrality of plasma, and conservation of the heavy particle number for every species. The full set of equations used to predict $X_{(s)}^{z**}$ and T^{**} is presented in Appendix 2. At the final stage of computations, values of X_i^z and $T_{e,i}$ for all simulated particles in the cell are updated with values of $X_{(s)}^{z**}$ for corresponding species and T^{**}, while the velocities of heavy particles are changed according to the equation

$$\mathbf{v}_i^{**} = \mathbf{u} + \left(\mathbf{v}_i^* - \mathbf{u}\right)\sqrt{\frac{T^{**}}{T^*}}. \tag{7}$$

This approach enforces thermalization of the whole system of particles in each cell by the end of the time step, so that $T_a^{**} = T_e^{**} = T^{**}$.

Appendix 2. Models of ionization and absorption of laser radiation

In this work, the simulations are performed based on the equilibrium model of ionization. This model is applied at each time step in every cell of the computational mesh in order to enforce the equilibrium degrees of ionization by the end of the time step. In every cell at each time step of the computational algorithm, we determine, based on parameters of individual simulated particles, the number densities of individual species n_s and total thermal energy density E (energy of the chaotic motion of all particles plus the energy of ionization per unit volume). The molar fraction of particles of species s with ion charge z, $X_{(s)}^z$, and temperature, T, are determined based on the solution of the Saha equations, e.g., [14]

$$\frac{n_e X_{(s)}^z}{X_{(s)}^{z-1}} = \left(\frac{2\pi m_e k_B T}{h^2}\right)^{3/2} \exp\left(-\frac{\mathrm{IP}_s^z}{k_B T}\right), \quad s = 1, 2,\ z = 1, \ldots, Z_{\max}, \tag{8}$$

where $n_e = \sum_s n_s \sum_z z X_{(s)}^z$, h is the Planck constant, and m_e is mass of an electron. Equation (8) is coupled with the energy conservation equation [14]

$$E = \sum_{s=1}^{2} n_s \left[\left(1 + \sum_{z=1}^{Z_{\max}} z X_{(s)}^z\right) k_B T + \sum_{z=1}^{Z_{\max}} IP_s^z X_{(s)}^z\right]. \tag{9}$$

Equations (8) and (9) at fixed E and n_s are solved iteratively with respect to T and $X_{(s)}^z$ using the Newton–Raphson method.

The values of T and $X_{(s)}^z$ are then used to calculate the plasma absorption coefficient α based on the model suggested in Ref. [33] in the form

$$\alpha = \sum_{s=1}^{2} \left(\alpha_{\mathrm{PI}(s)} + \alpha_{\mathrm{IB},i(s)} + \alpha_{\mathrm{IB},n(s)}\right), \tag{10}$$

where $\alpha_{\mathrm{PI}(s)}$, $\alpha_{\mathrm{IB},i(s)}$, and $\alpha_{\mathrm{IB},n(s)}$ accounts for the effects of photoionization and inverse Bremsstrahlung in electron collisions with ions and neutral atoms of species s:

$$\alpha_{\mathrm{PI}(s)} = \sum_{z=0}^{Z_{\max}} \sum_{j=N_{*(s)}^z}^{N_{\max(s)}^z} n_{j(s)}^z \sigma_{\mathrm{PI},j(s)}^z(T), \tag{11}$$

$$\alpha_{\mathrm{IB},i(s)} = \left[1 - \exp\left(-\frac{hc}{\lambda k_\mathrm{B} T}\right)\right]\sqrt{\frac{2\pi}{3m_\mathrm{e}k_\mathrm{B}T}}\frac{4e^6k_\mathrm{e}^3\lambda^3 n_\mathrm{e}n_s}{3hc^4m_\mathrm{e}}\sum_{z=1}^{Z_\mathrm{max}} z^2 X_{(s)}^z, \tag{12}$$

$$\alpha_{\mathrm{IB},n(s)} = \left[1 - \exp\left(-\frac{hc}{\lambda k_\mathrm{B} T}\right)\right]\sigma_{\mathrm{IB},n(s)}(T) n_\mathrm{e} n_s^0. \tag{13}$$

Here k_e is the Coulomb constant, c is the speed of light, j is the energy level, $N_{*(\mathrm{s})}^z = N_{*(\mathrm{s})}^z(\lambda)$ is the minimum energy level number of an ion of species s and charge z which can be further ionized to charge $z+1$ by absorbing a photon of wavelength λ, $N_{\mathrm{max}(s)}^z$ is the maximum energy level considered in calculations, and $n_{j(s)}^z$ is the number density of particles in energy level j, which is calculated based on the Boltzmann equilibrium distribution, $n_{j(s)}^z = n_{0(\mathrm{s})}^z\left(g_{j(s)}^z/g_{0(\mathrm{s})}^z\right)\exp\left[-\left(E_{j(s)}^z - E_{0(\mathrm{s})}^z\right)/\left(k_\mathrm{B}T\right)\right]$, where $g_{j(s)}^z$ and $E_{j(s)}^z$ are the statistical weight and energy at level j.

The photoionization cross section $\sigma_{\mathrm{PI},j}^z(T)$ is calculated as [33]

$$\sigma_{\mathrm{PI},j(s)}^z(T) = \frac{32\pi^2(z+1)^2e^6k_\mathrm{e}^3}{3\sqrt{3}h^4cv^3g_{j(s)}^Z}u_{(s)}^{z+1}(T)\frac{\mathrm{d}E_{j(s)}^z}{\mathrm{d}j}, \tag{14}$$

where $\nu = c/\lambda$ is the laser radiation frequency,

$$u_{(s)}^z(T) = \sum_{j=0}^{N_{\mathrm{max}(s)}^z} g_{j(s)}^z \exp\left(-\frac{E_{j(s)}^z - E_{0(s)}^z}{k_\mathrm{B}T}\right). \tag{15}$$

is the partition function, and $\mathrm{d}E_{j(s)}^Z/\mathrm{d}j$ is the spacing between energy levels. The electron-neutral collision cross section $\sigma_{\mathrm{IB},n(s)}(T)$ in Eq. (13) is calculated as suggested in Ref. [34]:

$$\sigma_{\mathrm{IB},n(s)}(T) = \int_0^\infty K_{a(s)}(E) f_\mathrm{MB}(E,T)\mathrm{d}E, \tag{16}$$

where

$$K_{\mathrm{a}(s)}(E) = \frac{2e^2k_\mathrm{e}}{3\pi m_\mathrm{e}cv^2}\sqrt{\left(\frac{2(E+h\nu)}{m_\mathrm{e}}\right)}\frac{E+h\nu}{h\nu}\sigma_{\mathrm{T}(s)}(E+h\nu), \tag{17}$$

$f_\mathrm{MB}(E,T) = 2\sqrt{E/\left(\pi\left(k_\mathrm{B}T\right)^3\right)}\exp\left[-E/\left(k_\mathrm{B}T\right)\right]$ is the Maxwell–Boltzmann distribution, and $\sigma_{\mathrm{T}(s)}(E)$ is the momentum transport cross section for electron-neutral collisions.

Based on preliminary simulations, the value of $Z_\mathrm{max} = 3$ is adopted for all simulations, since the molar fraction of triply ionized atoms does not exceed 1% under conditions considered in this work. The ionization energies are equal to $\mathrm{IP}_1^1 = 7.73$ eV, $\mathrm{IP}_1^2 = 20.29$ eV, and $\mathrm{IP}_1^3 = 36.84$ eV for copper [35] and $\mathrm{IP}_2^1 = 15.76$ eV, $\mathrm{IP}_2^2 = 27.63$ eV, and $\mathrm{IP}_2^3 = 40.74$ eV for argon [36]. The tables with energy levels and their statistical weights for copper and argon ions are adopted from Refs. [35, 36]. The values of the momentum transport cross section $\sigma_{\mathrm{T}(s)}(E)$ for copper and argon atoms in the tabulated form are taken from Refs. [37, 38], respectively, and then interpolated for calculations of $\sigma_{\mathrm{IB},n(s)}(T)$ according to Eqs. (16) and (17).

References

1. M.R.H. Knowles, G. Rutterford, D. Karnakis, A. Ferguson, Micromachining of metals, ceramics and polymers using nanosecond lasers. Int. J. Adv. Manuf. Technol. **33**, 95–102 (2007)
2. N.B. Dahotre, S.P. Harimkar, *Laser Fabrication and Machining of Materials* (Springer, New York, 2008)
3. D.W. Hahn, N. Omenetto, Laser-induced breakdown spectroscopy (LIBS), part I: Review of basic diagnostics and plasma—particle interactions: Still-challenging issues within the analytical plasma community. Appl. Spectrosc. **64**, 335A–336A (2010)
4. D.W. Hahn, N. Omenetto, Laser-induced breakdown spectroscopy (LIBS), part II: Review of instrumental and methodological approaches to material analysis and applications to different fields. Appl. Spectrosc. **66**, 347–419 (2012)
5. P.R. Willmott, J.R. Huber, Pulsed laser vaporization and deposition. Rev. Mod. Phys. **72**, 315–328 (2000)
6. P.M. Ossi, Cluster synthesis and cluster-assembled film deposition in nanosecond pulsed laser ablation, in *Laser-Surface Interactions for New Materials Production*, ed. by A. Miotello, P.M. Ossi (Springer, New York, 2010), pp. 99–124
7. K. Ding, L. Ye, *Laser Shock Peening: Performance and Process Simulation* (Woodhead Publishing Ltd., Cambridge, 2006)
8. N.M. Bulgakova, A.B. Evtushenko, Y.G. Shukhov, S.I. Kudryashov, A.V. Bulgakov, Role of laser-induced plasma in ultradeep drilling of materials by nanosecond laser pulses. Appl. Surf. Sci. **257**, 10876–10882 (2011)
9. J.A. Aguilera, C. Aragón, F. Peñalba, Plasma shielding effect in laser ablation of metallic samples and its influence on LIBS analysis. Appl. Surf. Sci. **127–129**, 309–314 (1998)
10. S.S. Harilal, Influence of spot size on propagation dynamics of laser-produced tin plasma. J. Appl. Phys. **102**, 123306 (2007)
11. X. Li, W. Wei, J. Wu, S. Jia, A. Qiu, The Influence of spot size on the expansion dynamics of nanosecond-laser-produced copper plasmas in atmosphere. J. Appl. Phys. **113**, 243304 (2013)
12. A.V. Bulgakov, N.M. Bulgakova, Dynamics of laser-induced plume expansion into an ambient gas during film deposition. J. Phys. D: Appl. Phys. **28**, 1710–1718 (1995)
13. G. Clair, D. L'Hermite, 1D modelling of nanosecond laser ablation of copper samples in argon at P = 1 atm with a wavelength of 532 nm. J. Appl. Phys. **110**, 083307 (2011)
14. Z. Chen, A. Bogaerts, Laser ablation of Cu and plume expansion into 1 atm ambient gas. J. Appl. Phys. **97**, 063305 (2005)
15. B. Wu, Y.C. Shin, Modeling of nanosecond laser ablation with vapor plasma formation. J. Appl. Phys. **99**, 084310 (2006)
16. T.E. Itina, J. Hermann, P. Delaporte, M. Sentis, Laser-generated plasma plume expansion: Combined continuous-microscopic modeling. Phys. Rev. E **66**, 066406 (2002)
17. T.E. Itina, F. Vidal, P. Delaporte, M. Sentis, Numerical study of ultra-short laser ablation of metals and of laser plume dynamics. Appl. Phys. A **79**, 1089–1092 (2004)
18. K. Choudhury, R.K. Singh, S. Narayan, A. Srivastava, A. Kumar, Time resolved interferometric study of the plasma plume induced shock wave in confined geometry: Two-dimensional mapping of the ambient and plasma density. Phys. Plasma **23**, 042108 (2016)

19. Y. Wang, H. Yuan, Y. Fu, Z. Wang, Experimental and computational investigation of confined laser-induced breakdown spectroscopy. Spectrochim. Acta Part B **126**, 44–52 (2016)
20. H.C. Le, D.E. Zeitoun, J.D. Parisse, M. Sentis, W. Marine, Modeling of gas dynamics for a laser-generated plasma: Propagation into low-pressure gases. Phys. Rev. E **62**, 4152–4161 (2000)
21. A.C. Forsman, P.S. Banks, M.D. Perry, E.M. Campbell, A.L. Dodell, M.S. Armas, Double-pulse machining as a technique for the enhancement of material removal rates in laser machining of metals. J. Appl. Phys. **98**, 033302 (2005)
22. Q. Min, M.G. Su, B. Wang, L. Wu, S.Q. He, D.X. Sun, S.Q. Cao, C.Z. Dong, Investigation of the expansion dynamics of silicon plasmas generated by double nanosecond laser pulses. Phys. Plasmas **25**, 073302 (2018)
23. B. Tan, Deep micro hole drilling in a silicon substrate using multi-bursts of nanosecond UV laser pulses. J. Micromech. Microeng. **16**, 109–112 (2006)
24. A. Bogaerts, Z. Chen, D. Autrique, Double pulse laser ablation and laser induced breakdown spectroscopy: A modeling investigation. Spectrochim. Acta Part B **63**, 746–754 (2008)
25. O.A. Ranjbar, Z. Lin, A.N. Volkov, One-dimensional kinetic simulations of plume expansion induced by multi-pulse laser irradiation in the burst mode at 266 nm wavelength. Vacuum **157**, 361–375 (2018)
26. G.A. Bird, *Molecular Gas Dynamics and the Direct Simulation of Gas Flows* (Oxford University Press, New York, 1994)
27. M.N. Kogan, *Rarefied Gas Dynamics* (Plenum Press, New York, 1969)
28. C. Cercignany, *Rarefied Gas Dynamics: From Basic Concepts to Actual Calculations* (Cambridge University Press, Cambridge, 2000)
29. A.N. Volkov, G.M. O'Connor, T.J. Glynn, G.A. Lukyanov, Expansion of a laser plume from a silicon wafer in a wide range of ambient gas pressures. Appl. Phys. A **92**, 927–932 (2008)
30. A. Palya, O.A. Ranjbar, Z. Lin, A.N. Volkov, Effect of the background gas pressure on the effectiveness of laser-induced material removal from deep cavities in irradiated targets. Appl. Phys. A **124**, 32 (2018)
31. A. Palya, O.A. Ranjbar, Z. Lin, A.N. Volkov, Kinetic simulations of laser-induced plume expansion into a background gas under conditions of spatial confinement. Int. J. Heat Mass Transf. **132**, 1029–1052 (2019)
32. N. Arnold, J. Gruber, J. Heitz, Spherical expansion of the vapor plume into ambient gas: An analytical model. Appl. Phys. A **69**, S87–S93 (1999)
33. D. Autrique, V. Alexiades, Comment on "Laser ablation of Cu and plume expansion into 1 atm ambient gas" [J. Appl. Phys. 97, 063305 (2005)]. J. Appl. Phys. **115**, 166101 (2014)
34. Y.B. Zel'dovich, Y.P. Raizer, *Physics of Shock Waves and High-Temperature Hydrodynamic Phenomena* (Dover, New York, 2013)
35. J. Sugar, A. Musgrove, Energy levels of copper, Cu I through Cu XXIX. J. Phys. Chem. Ref. Data **19**, 527–616 (1990)
36. E.B. Saloman, Energy levels and observed spectral lines of ionized argon, Ar II through Ar XVIII. J. Phys. Chem. Ref. Data **39**, 033101 (2010)
37. O. Zatsarinny, K. Bartschat, Electron collisions with copper atoms: Elastic scattering and electron-impact excitation of the $(3d^{10}4s)^2S \rightarrow (3d^{10}4p)^2P$ resonance transition. Phys. Rev. A **82**, 062703 (2010)
38. Y. Nakamura, M. Kurachi, Electron transport parameters in argon and its momentum transfer cross section. J. Phys. D: Appl. Phys. **21**, 718–723 (1988)